Article

Monolithic 3D integration of tantalum pentoxide nonlinear photonics

https://doi.org/10.1038/s41586-026-10379-w

Received: 28 August 2025

Accepted: 9 March 2026

Published online: 15 April 2026

Check for updates

Grant M. Brodnik[1]✉, Grisha Spektor[2], Lindell M. Williams[1,3], Jizhao Zang[1,3], Alexa R. Carollo[1], Atasi Dan[1,3], Jennifer A. Black[1], David R. Carlson[2] & Scott B. Papp[1,3]

The photonics landscape encompasses a wide scope of material platforms, each optimized for specific functionalities, yet no platform meets the demands of all current and evolving photonic applications. Although combining integrated-photonics materials enhances overall capability, such as unifying nonlinear optics, low-loss passive devices and electro-optics, material and process compatibility remains a major challenge. Here we introduce full-wafer, monolithic 3D integration of tantalum pentoxide (Ta_2O_5, hereafter tantala[1]) photonics directly onto a patterned substrate, demonstrated here with thin-film lithium niobate[2]. Tantala's unique properties, importantly room-temperature deposition, moderate-temperature annealing and low residual stress in thick films optimized for phase matching, make it well suited for monolithic 3D integration without compromising substrate performance or compatibility. We demonstrate low-loss, high-quality-factor microresonators and nanophotonics in tantala, robust quasi-phase-matching in poled lithium niobate waveguides[3], and efficient 3D interlayer routing. These capabilities enable us to demonstrate a rich palette of nonlinear frequency conversion processes, including $\chi^{(3)}$ four-wave mixing for supercontinuum generation, optical parametric oscillation and dark-pulse microcomb generation in tantala microresonators and photonic crystal resonators, $\chi^{(2)}$ second-harmonic generation in periodically poled lithium niobate, and combinations thereof.

The advancement of integrated photonics has the potential to fuel innovation across a broad range of applications including metrology[4], telecommunications[5], visible-light consumer electronics[6] and quantum technologies[7]. These examples highlight the diverse functional demands placed on photonic systems, requiring laser sources, frequency combs, high-speed modulators and quantum light sources in single platforms. For higher performance and capabilities that meet these demands, recent efforts have focused on bringing nonlinear optics on-chip. Third-order nonlinear $\chi^{(3)}$ platforms such as silicon nitride (SiN)[8–10], tantalum pentoxide (Ta_2O_5, hereafter tantala)[1,11,12] and aluminium nitride[13] support a range of efficient nonlinear phenomena including frequency-comb generation, supercontinuum generation, soliton dynamics and broadband wavelength conversion. Thin-film second-order nonlinear $\chi^{(2)}$ systems using materials such as lithium niobate (LN)[2,14,15], lithium tantalate[16] and barium titanate (BTO)[17] enable high-bandwidth electro-optic modulation[18] and second-harmonic generation (SHG), often through quasi-phase-matched poled waveguides[3,19–21]. Nonetheless, despite significant progress in both established and emerging platforms, it is widely recognized that no single material can satisfy all functional requirements. As a result, efforts are increasingly focused on strategies that combine integrated-photonics platforms with high-performance nonlinear materials, particularly those supporting broadband low-loss across the visible and shortwave infrared, to unlock the potential of integrated photonics.

Heterogeneous integration has emerged as a strategy for uniting complementary photonic materials. By bonding entirely separate substrates with distinct materials for optical, electronic and structural properties, such as integrating III–V semiconductors with low-loss passive and nonlinear waveguides, this approach enables the realization of complex, multifunctional photonic systems[22–24]. Recent demonstrations have combined III–V gain media with nonlinear waveguides to realize integrated amplifiers and tunable lasers[25,26] and microresonator frequency combs[27] pumped by on-chip lasers. Other integration efforts have leveraged techniques such as micro-transfer printing[28] and direct bonding[29–31] to combine thin-film LN and SiN platforms. The techniques used in these approaches stem from SiN material properties and processing conditions required to produce low-loss, thick-film photonic layers. Specifically, high residual stress (approximately 800 MPa), high-temperature deposition (approximately 770 °C) and high-temperature annealing (approximately 1,200 °C) of standardized recipes necessitate independent SiN wafer processing and additional steps in integration such as incorporating stress-relief structures[9,10]. Indeed, although heterogeneous integration developments are promising within select material ecosystems, the need for recurring customization of fabrication to ensure material and process compatibility poses a significant barrier to scalability and therefore broader adoption with arbitrary photonic ecosystems.

[1]Time and Frequency Division, National Institute of Standards and Technology, Boulder, CO, USA. [2]Octave Photonics, Louisville, CO, USA. [3]Department of Physics, University of Colorado Boulder, Boulder, CO, USA. ✉e-mail: grant.brodnik@nist.gov

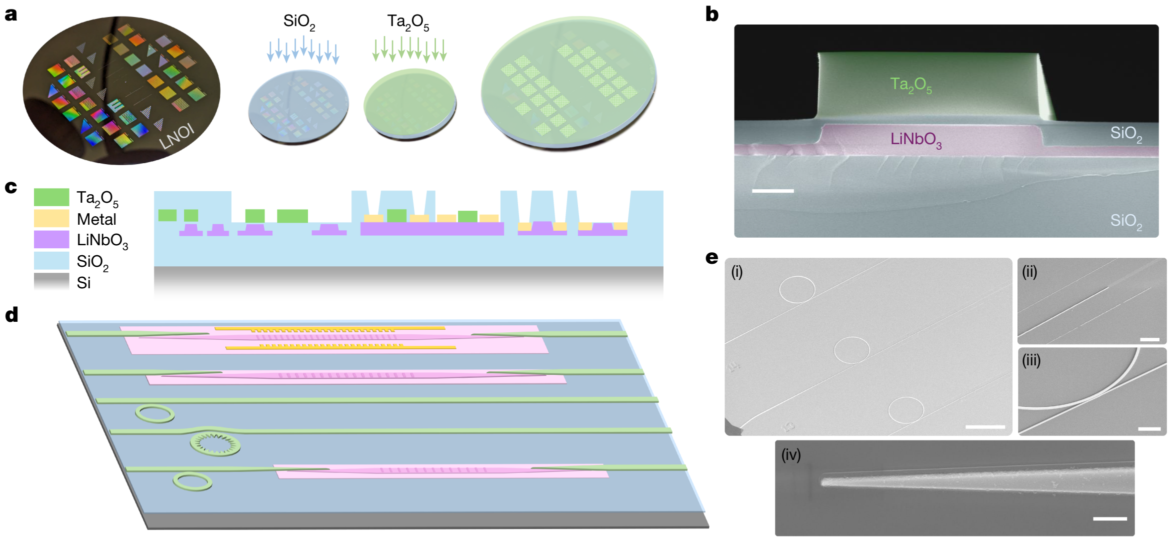

Fig. 1 | Monolithic 3D integration of tantala photonics on patterned substrates. a, The tantala–LN platform is realized by depositing tantala onto a commercial thin-film LNOI wafer, facilitated using a planarized SiO_2 interface layer. **b**, SEM image of tantala–LN cross-section. **c**, Tantala–LN waveguide configurations and optional metal integration. **d**, Tantala–LN device palette comprising poled LN waveguides, high-Q tantala microresonators and PhCRs with 3D interlayer routing afforded by taper structures. **e**, SEM images of tantala resonators (i), an interlayer taper transition between tantala and LN (ii), a tantala ring-bus coupler (iii) and a close-up of a tantala taper (iv). Scale bars, 400 nm (**b**); 100 μm (**e**(i)); 10 μm (**e**(ii),(iii)); 1 μm (**e**(iv)).

Monolithic integration presents a streamlined and scalable path to combine materials and realize diverse functionalities within a unified platform and fabrication process. Originating in microelectronics, it involves sequential fabrication of multiple device layers on a common substrate within a cohesive process flow. This approach underpins complementary metal–oxide–semiconductor (CMOS) technology, where transistors, interconnects and memory are vertically integrated at the wafer level to deliver dense and cost-effective circuits. In photonics, early monolithic efforts on indium phosphide (InP) platforms[32] demonstrated integration of active and passive components such as lasers, modulators and photodetectors into a single chip, enabling compact optical transceivers and high-bandwidth communication systems. Silicon photonics subsequently advanced monolithic strategies by incorporating vertically stacked silicon-on-insulator waveguide layers to increase routing density and device functionality within foundry-scale processes[33]. More recently, monolithic three-dimensional (3D) photonic integration has emerged, particularly in silicon-on-insulator and SiN platforms, where multiple photonic layers are stacked and interconnected[34,35]. Monolithic integration supports tailoring of individual layers for specific optical properties such as dispersion, transparency range or nonlinear response while maintaining lithographic alignment and low-loss interlayer transitions. By preserving full-wafer-scale compatibility and avoiding intermediate assembly steps, monolithic integration offers a manufacturable framework to combine high-performance nonlinear functionality with complementary active and passive photonic devices, pointing towards unified material platforms.

Here we introduce monolithic 3D integration of tantala integrated photonics directly on a thin-film LN photonic substrate, leveraging ultralow loss across the visible and near-infrared plus nonlinear and nanophotonic functionality. Monolithic 3D integration is made possible by the material properties of tantala that lend room-temperature, ion-beam-sputtering (IBS) deposition, low residual stress (38 MPa (ref. 1)), and moderate-temperature (500 °C) anneals or anneal-free variations using metal-oxide mixtures[36]. These advantages of tantala over, for example, SiN afford our monolithic 3D integration approach broad compatibility with underlying photonic materials and structures. We demonstrate seamless integration by realizing a tantala–LN platform, choosing commercial thin-film LN on Si as the substrate for its appeal as a $\chi^{(2)}$ and electro-optic visible photonics platform that affords nonlinear operation when paired with $\chi^{(3)}$ tantala. We present ultralow loss, 3D integrated circuits of tantala–LN, demonstrating interlayer routing[34] that enables upper-layer tantala photonics to efficiently interface lower-layer LN devices. We verify low-loss waveguide fabrication by measuring microresonators with intrinsic quality factors (Q_i) exceeding 5 million and characterize high-Q photonic crystal resonators (PhCRs)[37–39], demonstrating platform support for nanophotonic designs. Finally, we showcase $\chi^{(3)}$ and $\chi^{(2)}$ tantala–LN operation with four-wave-mixing (FWM) optical parametric oscillation (OPO) and dark-pulse microcomb generation on upper-layer tantala and SHG in lower-layer periodically poled LN. We leverage the $\chi^{(3)}$ and $\chi^{(2)}$ nonlinearities of tantala–LN in series-connected, dual-layer devices for broadband, arbitrary-wavelength laser conversion using OPO with SHG and for carrier-envelope offset frequency (f_{ceo}) detection of comb sources using tantala supercontinuum generation followed by SHG in LN for f–$2f$ self-referencing[40,41]. Our results demonstrate monolithic 3D tantala integration as a remarkable paradigm for scalable, multifunctional photonic systems, enabling incorporation of nonlinear optics directly into existing and emerging photonics infrastructure.

Monolithic 3D Integration of tantala

Figure 1 presents monolithic 3D integration for realizing tantala photonics on patterned substrates. Our process uses room-temperature IBS of tantala to leverage a mix of capabilities for monolithic integration, such as precise control of tantala films onto substrates and amenability to doping with, for example, metal-oxide mixtures to tailor material properties and afford anneal-free processing[36]. Figure 1a explores the flexibility of monolithic 3D integration with thin-film LN-on-insulator (LNOI) as the lower substrate, realizing the tantala–LN platform. Figure 1b shows a cross-section scanning electron microscope (SEM) image of an example structure in which a tantala waveguide is realized directly on top of an etched LN waveguide. In this image, the bottom oxide and the LN layer are components of the commercial LNOI wafer, and the upper oxide is the planarized interface layer. Here the LN layer is partially etched to realize a specific device design, but full layer etching is also possible. The upper-layer tantala waveguides shown in the

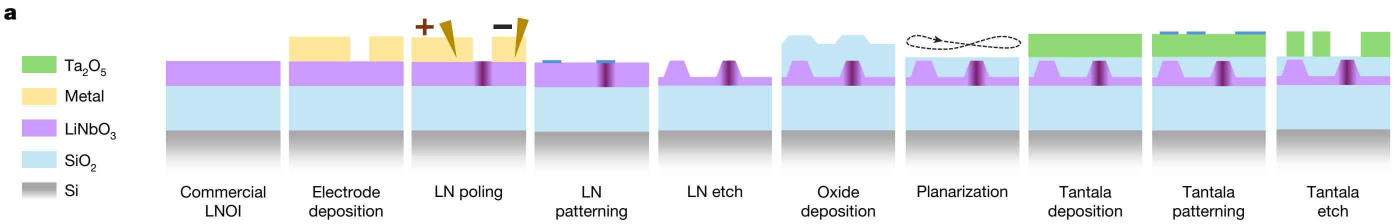

b

Ta_2O_5 (tantala)

n	2.23–2.05	(400–2,000 nm)
n_2	6.2×10^{-19}	$m^2\ W^{-1}$
dn/dT	8.8×10^{-6}	K^{-1}
Stress	38	MPa
E_{BG}	3.8	eV
T_{dep}	25	°C
T_{anneal}	500	°C

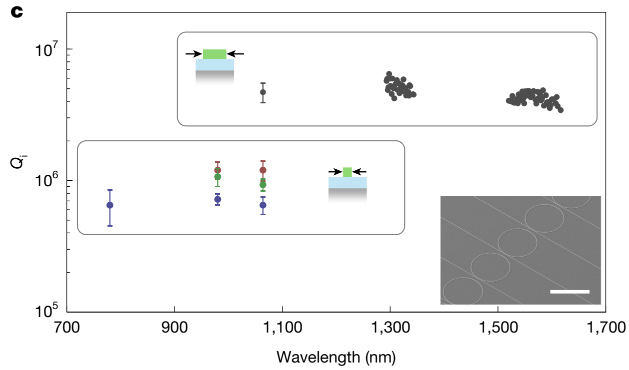

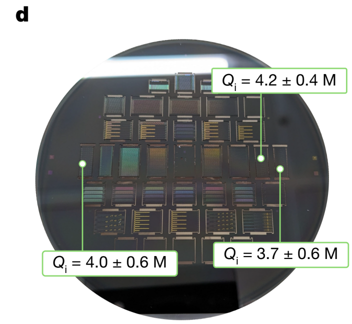

Fig. 2 | Tantala–LN fabrication, tantala material properties and microresonator *Q*. a, Process flow for monolithic 3D integrated tantala photonics realized directly on commercialized thin-film LNOI substrates. **b**, Material parameters (n, refractive index; n_2, nonlinear refractive index; dn/dT, thermo-optic coefficient, where T is temperature; E_{BG}, material bandgap; T_{dep}, tantala deposition temperature; T_{anneal}, anneal temperature) relevant for tantala nonlinear photonics fabrication and operation[1,11,12,43]. **c**, Measured intrinsic quality factor (Q_i) of wide ring width, normal dispersion (top; ring width 4 µm) and narrow ring width, near-zero dispersion (bottom; ring width 890 µm, 1,040 µm and 1,140 µm in blue, green and red, respectively) microresonators fabricated on the tantala–LN platform. Error bars indicate standard deviation across multiple resonance measurements of the same device. Inset shows an SEM image of fabricated tantala microresonators. **d**, A 3-inch tantala–LN wafer image identifying Q_i, measured at 1,550 nm, for microresonators of the same design from 3 separate chips at different locations on the wafer. Scale bar, 90 µm (**c**, inset).

SEM image are designed for air-cladding to realize high-index-contrast operation for the visible-wavelength band. This image qualitatively assesses waveguide fabrication and alignment precision realized by monolithic tantala processing, thereby demonstrating capabilities for direct, co-integration of two distinct waveguide layers.

In Fig. 1c, we show a range of waveguide designs supported by monolithic 3D tantala–LN integration in terms of material layers, claddings and optional metallization for poling electrodes, electro-optic control and heaters. The platform leverages the complementary optical properties of tantala and LN, specifically, broadband transparency from the upper edge of the ultraviolet to shortwave infrared and comparable refractive indices that support high-index-contrast waveguides and efficient mode-matching between waveguides[11,12,42]. Together, the material properties and the layout circuit possibilities create the functionality to access a rich nonlinear design space (Fig. 1d). Figure 1e shows SEM images of tantala microresonators, an interlayer taper structure, a tantala ring-bus coupler and a close-up of a single taper.

Fabrication and passive characteristics

We outline the tantala–LN wafer fabrication in Fig. 2a, beginning with commercial, 300-nm-thick magnesium-oxide-doped X-cut LN film on a 3-inch oxidized silicon (Si) wafer. Our process begins with patterning the LN layer, followed by inductively coupled plasma chemical vapour deposition and planarization of silicon dioxide (SiO_2), then IBS and patterning of the tantala layer. The ultrathin, planarized oxide layer enables a low-loss interface between tantala photonics with the lower substrate. Complete fabrication details are provided in Methods. In Fig. 2b, we summarize tantala material parameters relevant to photonic performance and fabrication[1,11,12]. In terms of nonlinear performance, we note the strong nonlinear coefficient of tantala (6.2×10^{-19} $m^2\ W^{-1}$ measured at 1,550 nm (ref. 1) and 7.23×10^{-19} $m^2\ W^{-1}$ measured at 800 nm (ref. 43)), compared with SiN (2.4×10^{-19} $m^2\ W^{-1}$ measured at 1,550 nm (ref. 44)).

We experimentally characterize optical loss, as low-loss waveguides and high-Q resonators are critical for efficient nonlinear operation. For example, in microresonator-based FWM processes, threshold power scales inversely with the square of loaded Q (Q_L)[45] and integrated devices aim for operation with practical on-chip pump powers. To support high Q_L, a photonics platform must fundamentally support high Q_i, as Q_L is dependent on coupling Q (Q_c) via ring-bus coupling designs and through the relation $Q_L^{-1} = Q_c^{-1} + Q_i^{-1}$. We measure microresonator Q_i on the tantala–LN platform by performing microresonator spectroscopy of dispersion engineered, wide- and narrow-ring-width designs in Fig. 2c. We use tunable lasers at multiple wavebands to measure transmission of device resonances in parallel with a calibrated fibre Mach–Zehnder interferometer, using the Mach–Zehnder interferometer transmission as an optical frequency ruler. The devices we characterize are designed for operation using the fundamental transverse electric mode (TE0), although designs that use other polarization or waveguide modes[46] are possible. We fit experimental transmission data to extract Q_i and calculate waveguide loss, α, in microresonators with a ring width of 4 µm optimized for normal dispersion 200-GHz dark-pulse generation and microresonators with narrow ring width designed for near-zero dispersion broadband OPO. In 4-µm devices (Fig. 2c, top), we measure Q_i to be approximately 4.7×10^6 ($\alpha = 0.12$ dB cm^{-1}), approximately 5.5×10^6 ($\alpha = 0.09$ dB cm^{-1}) and approximately 4.5×10^6 ($\alpha = 0.09$ dB cm^{-1}) for wavelengths of 1,064 nm, 1,310 nm and 1,550 nm, respectively. In narrow-ring-width devices (Fig. 2c, bottom), we measure Q_i between approximately 7.5×10^5 and approximately 1.2×10^6 for ring widths of 890 nm (blue), 1,040 nm (green) and 1,140 nm (red) at wavelengths between 780 nm and 1,064 nm. The Q_i values for the narrowest waveguide device (ring width 890 nm) correspond to waveguide losses of $\alpha = 1.2$ dB cm^{-1}, $\alpha = 0.9$ dB cm^{-1} and $\alpha = 0.9$ dB cm^{-1} for wavelengths of 780 nm, 980 nm and 1,064 nm, respectively. The dependence of Q_i and α on ring width suggests that optical loss is limited by waveguide scattering owing to increased modal overlap with side walls in narrower devices.

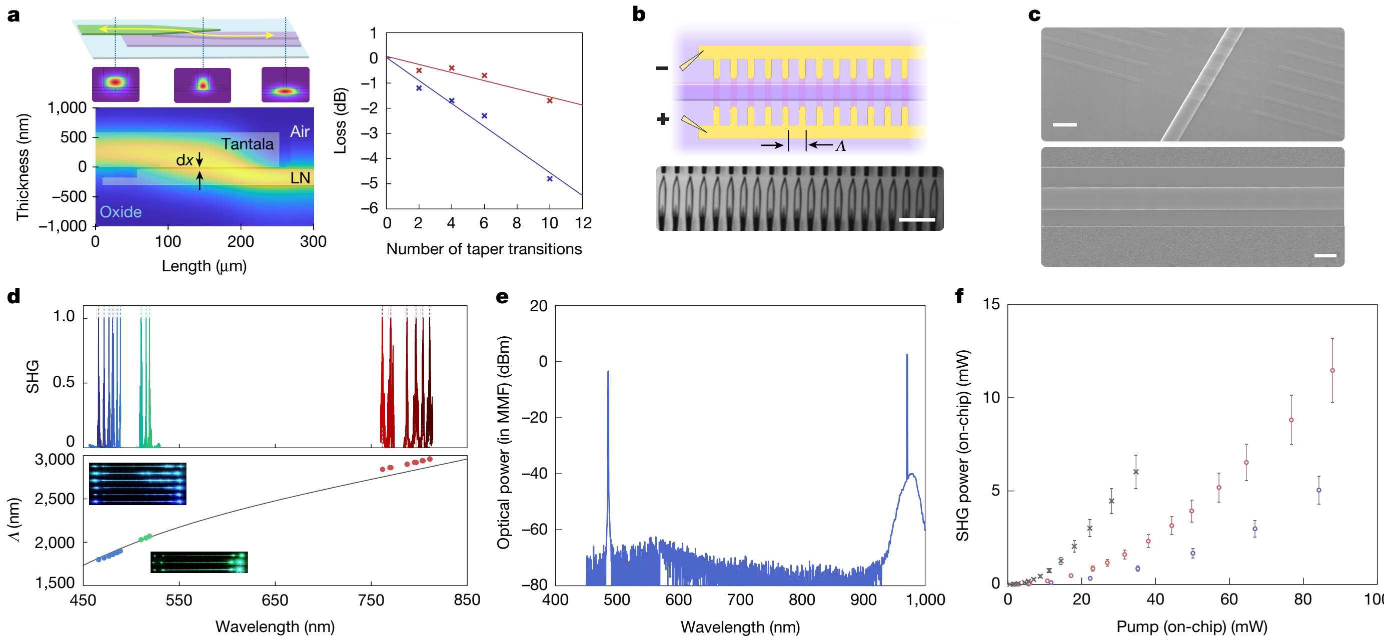

Fig. 3 | Tantala–LN interlayer routing and SHG. a, Left: interlayer taper schematic, simulated mode profiles at points in the taper transition and 3D modelled TE0 electric field showing transmission from upper-layer tantala to lower-layer LN. Right: measured loss of taper transition test structures at 1,550 nm (red) and 780 nm (blue). **b**, Schematic of LN poling electrodes (top) and second-harmonic microscope image showing domain inversion of poled regions (bottom). **c**, SEM images of a poled and etched LN waveguide before (top) and after (bottom) removing residual electrode patterning. **d**, Normalized SHG gain spectrum versus wavelength for devices with varying Λ (top). Comparison with modelled (black line) phase matching and images of tested devices during operation (bottom). **e**, Optical spectrum of a tantala–LN SHG device converting a 970-nm pump to 485-nm signal, measured directly from multimode fibre (MMF) edge-coupled to output facet. **f**, Calibrated on-chip pump power versus on-chip SHG power for an LNOI device with output SHG of 525 nm (grey crosses) and tantala–LN devices with output SHG of 485 nm (blue circles) and 787 nm (red circles). Error bars indicate standard deviation uncertainty in on-chip SHG power based on propagated uncertainty of chip insertion loss measurements. Scale bars, 5 μm (**b**, bottom); 3 μm (**c**, top); 2 μm (**c**, bottom).

Nonlinear operation

We explore design and operation of tantala–LN devices, demonstrating a complete palette of $\chi^{(2)}$ and $\chi^{(3)}$ nonlinear optics and circuit combinations. We first explore SHG in $\chi^{(2)}$ periodically poled LN waveguides, especially through generation of visible light, and in 3D tantala–LN devices, where light is routed between tantala and LN layers to demonstrate interlayer functionality. In $\chi^{(3)}$ tantala, we demonstrate efficient FWM processes that realize ultrabroadband OPO in near-zero dispersion microresonators and dark-pulse generation in normal dispersion PhCRs[47]. Finally, we demonstrate cascaded $\chi^{(3)}$–$\chi^{(2)}$ operation by cascading upper-layer tantala microresonator OPO and straight waveguide supercontinuum generation to poled LN waveguides in single devices.

Figure 3a characterizes passive tantala–LN interlayer routing structures, which leverage adiabatic, coupled tapering techniques broadly suited to low-loss optical mode transitions[34]. The taper regions are 250 μm in total length, with linearly decreasing waveguide widths from 2 μm down to 150 nm for both the tantala and LN waveguides. We show a 3D schematic (exaggerated dimensions to show features) and a 2D slice labelling the silica interface thickness, dx, dependent on chemical-mechanical polishing (CMP) planarization, overlaid with a sample finite-difference-time-domain simulation in Fig. 3a (left). Our e-beam lithography process is suited for high-precision alignment of taper structures, with a specified precision of ±20 nm. More critical in terms of processing is the CMP oxide planarization step, which controls dx between the waveguides and affects modal overlap of the taper structures. Furthermore, modal overlap in general includes a wavelength dependence owing to the stronger confinement of optical modes at shorter wavelengths[34]. In finite-difference-time-domain simulations with dx = 150 nm, we found the loss per transition to be <0.05 dB at 1,550 nm and 0.3 dB at 780 nm. For dx = 200 nm, we simulate the loss per transition to be <0.05 dB at 1,550 nm, decreasing to 1.5 dB at 780 nm. We measure loss per transition in serially cascaded taper test structures to be below approximately 0.2 dB and approximately 0.5 dB for wavelengths of 1,550 nm (red) and 780 nm (blue), respectively (Fig. 3a, right).

In Fig. 3b–f, we explore nonlinear $\chi^{(2)}$ SHG in dual-layer tantala–LN devices enabled by the low-loss interlayer transitions. Figure 3b presents a schematic of poling electrodes centred about a LN waveguide where we define poling pitch, Λ, which controls quasi-phase-matching (QPM) and SHG gain wavelength. Throughout the poling procedure, we visually monitor domain inversion using a second-harmonic microscope. In the second-harmonic microscope image in Fig. 3b (bottom), poling electrodes are seen as dark fringes along the top and bottom, and inverted domains as the segments spanning the middle. Qualitatively, uniform colouring within each domain suggests complete poling through LN films and fixed repetition across domains shows longitudinal uniformity[20,48]. We show SEM images of poled devices following waveguide etching in Fig. 3c. Residual electrode material is observed on either side of the waveguide, but at distances sufficiently far from the waveguide to avoid interaction with optical modes.

We characterize wavelength-dependent phase matching in devices that target a range of visible SHG wavelengths by varying Λ (Fig. 3d). The devices are selected from two separate chips on the same tantala–LN wafer, one chip having devices poled for pump wavelengths spanning about 920–980 nm (blue curves and dots) and the other for about 1,020–1,050 nm (green curves and dots). Experimentally, we couple pump light into the chip using a lensed fibre with a spot size of 2 μm and collect SHG light out of the chip by edge coupling a multimode fibre directly to the chip facet (Methods). We tune the wavelength of the pump laser across the range of designed QPM targets and use an optical power meter with shortpass dichroic filters, cut at 750 nm

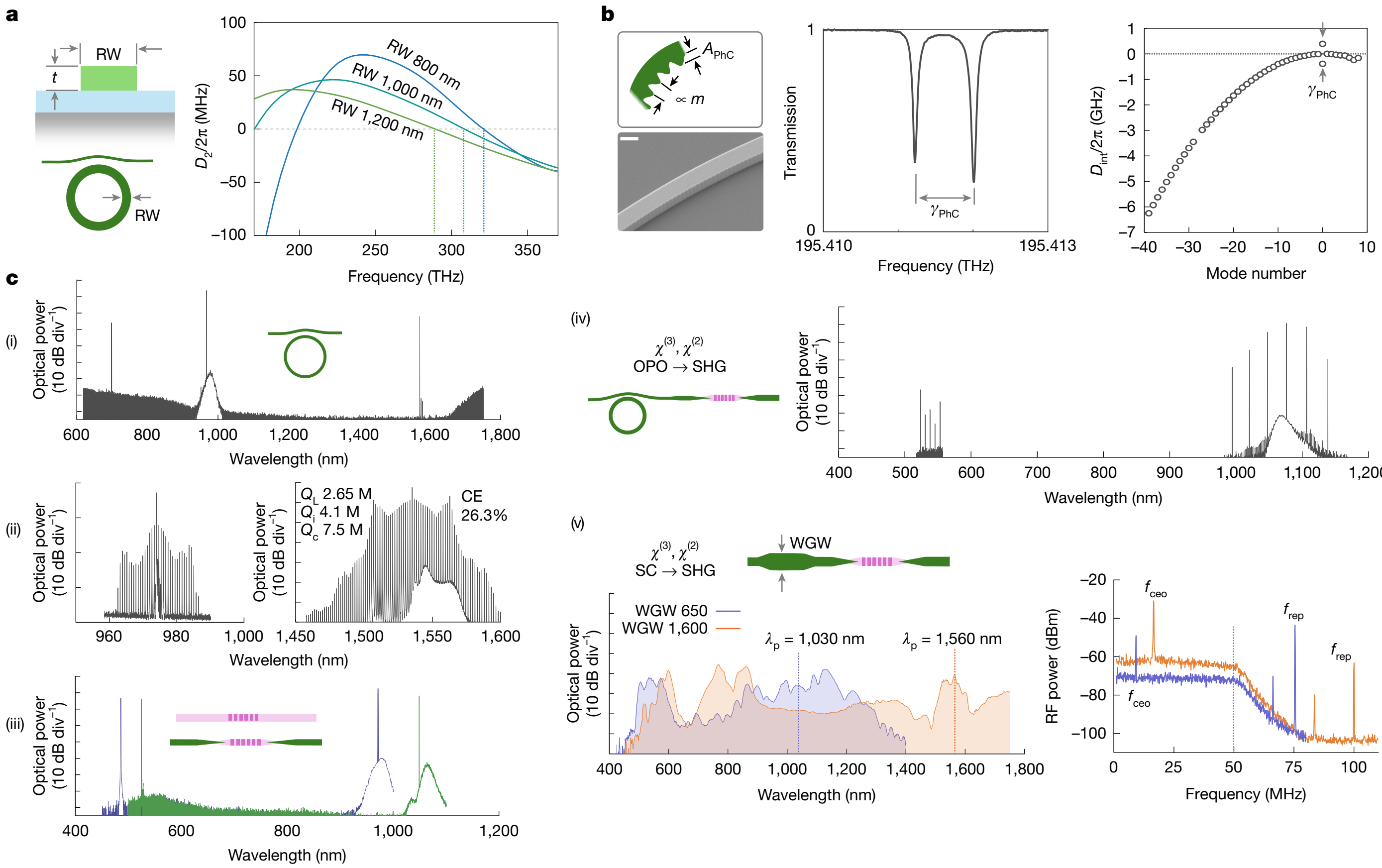

Fig. 4 | Tantala–LN $\chi^{(3)}/\chi^{(2)}$ designs and demonstrations. a, Geometric dispersion engineering and control of second-order dispersion parameter, D_2, realized by designing waveguide thickness, t, and ring width, RW. **b**, Photonic crystal design showing SEM image (left), measured resonator mode split, γ_{PhC} (middle) and integrated dispersion of a negative D_2 device with photonic crystal on the pump mode (right). Scale bar, 1 µm. **c**, Summary of nonlinear operation realized in 3D tantala–LN photonics: broadband wavelength conversion in near-zero dispersion tantala microresonator OPO (i), dark-pulse generation in normal dispersion tantala PhCRs operated with pump wavelengths of 972 nm (left) and 1,535 nm (right) with conversion efficiency (CE) for a representative 1,550 nm device indicated (ii), SHG in LNOI and 3D tantala–LN using poled LN waveguides (iii), cascaded $\chi^{(3)}$ OPO in tantala to $\chi^{(2)}$ SHG in lower LN (iv) and cascaded $\chi^{(3)}$ supercontinuum (SC) generation in tantala to $\chi^{(2)}$ SHG in LN (v). The tantala waveguide width, WGW, lends dispersion control for SC generation (left). Together with SHG, this device enables radiofrequency (RF) carrier-envelope offset (f_{ceo}) detection, which along with repetition rate (f_{rep}) detection, affords f–$2f$ self-referencing[40] for custom-pump-wavelength (λ_p) pulsed sources (λ_p = 1,030 nm in blue and λ_p = 1,560 nm in orange) (right).

with extinction exceeding 70 dB, to record SHG power versus wavelength. We plot the measured SHG gain spectrum for each Λ design (solid lines) and the calculated gain centres of mass (dotted lines) in the top of Fig. 3d. In the bottom of Fig. 3d, we plot the extracted gain centres of mass for each Λ along with the modelled phase-matching curve (black line). We note offsets in the measured SHG phase matching data against the modelled curve when comparing the three chips, which were fabricated at varied locations across the tantala–LN wafer. Furthermore, we note deviations from theoretical sinc-squared SHG gain, suggesting deviations in phase matching along the waveguide in single devices. Such effects have been explored in the literature and attributed to thickness variations in LNOI films, which could be addressed in future fabrication runs by adaptively biasing Λ designs based on wafer-level thickness measurements[49,50].

We next characterize tantala–LN SHG devices and a comparison LNOI SHG device operating under high-power pump conditions to assess performance in terms of power and efficiency. We show a sample spectrum of a tantala–LN 485-nm SHG device in Fig. 3e. In Fig. 3f, we plot the calibrated on-chip pump power versus SHG power of the LNOI device designed for an SHG target of 550 nm with device length, L, of 2,000 µm, and of tantala–LN devices for SHG targets of 485 nm and 787 nm, both with L = 1,800 µm.

We measure on-chip SHG power exceeding 6 mW for an on-chip pump power of 35 mW in the LNOI device, SHG power exceeding 5 mW for a pump power of 84 mW in the 485-nm tantala–LN device, and SHG power of 11 mW for a pump power of 87 mW in the 787-nm tantala–LN device. We calculate the geometry-normalized conversion efficiency to be 13,000% W^{-1} cm^{-2} for the LN device, 2,200% W^{-1} cm^{-2} for the 485-nm tantala–LN device, and 4,500% W^{-1} cm^{-2} for the 787-nm tantala–LN device. We attribute variations in performance between the devices to deviations in phase matching based on our characterization of SHG gain presented above in Fig. 3d.

Figure 4 explores $\chi^{(3)}$ and paired $\chi^{(3)}$–$\chi^{(2)}$ devices in monolithically integrated tantala–LN, which draw on the transition of previously developed tantala microresonator and PhCR designs[38,51,52]. In $\chi^{(3)}$ devices realized in upper-layer air-clad tantala, we use 570-nm-thick films that support strong mode confinement for high nonlinear gain and designable dispersion for controlling nonlinear phase matching. We characterize geometric control of phase matching by simulating group-velocity dispersion (GVD) for varied microresonator waveguide geometries that realize normal, near-zero and anomalous GVD across near-infrared pump laser frequencies (Fig. 4a). To link geometric dispersion engineering with practical designs, we identify the near-zero dispersion crossing (dotted lines) for each ring width, highlighting the operating point that realizes ultrabroadband-wavelength conversion based on tantala microresonator OPO.

Next, we explore nanophotonic PhCR designs that leverage nanometre-scale-resolution etching of tantala to control the bandgap mode and magnitude, lending mode-wise control of phase matching independent of broad geometric dispersion. We present a PhCR design in Fig. 4b, noting m as the parameter that affords mode selectivity via Bragg matching and A_{PhC} as a parameter that controls bandgap magnitude, γ_{PhC}. We show an SEM image of a fabricated PhCR device in Fig. 4b (bottom left). We measure γ_{PhC} in Fig. 4b (middle) and the integrated dispersion, D_{int} (Fig. 4b, right). The combination of normal GVD, realized through design of ring width, and phase-matching for FWM realized through design of the pump-mode bandgap enables dark-pulse generation for high-efficiency and spectrally flattened microcombs[47,53].

In Fig. 4c, we present experimental measurements that characterize a palette of $\chi^{(3)}$ and $\chi^{(2)}$ nonlinear photonics on the tantala–LN platform. These experiments encompass major themes in the recent development of integrated nonlinear photonics for the generation of unique sources including soliton microcombs, SHG, broadband OPOs, supercontinuum and combinations thereof. We schematically show tantala–LN circuits and their measured output optical spectra.

In a tantala microresonator designed for near-zero dispersion via geometric control (Fig. 4a), we demonstrate wavelength conversion that exceeds an octave of optical bandwidth from a pump wavelength of 968 nm to signal and idler wavelengths of 698 nm and 1,572 nm, respectively (Fig. 4c(i)). In a normal dispersion microresonator, and the normal dispersion PhCR presented in Fig. 4b, we show dark-pulse generation at pump wavelengths of 974 nm and 1,535 nm, respectively (Fig. 4c(ii)). For the 1,535 nm PhCR device shown in Fig. 4c(ii), we measure a conversion efficiency exceeding 26%. In Fig. 4c(iii), we show SHG in the LNOI device poled for 1,050–525 nm SHG, and in the tantala–LN device for 970–485 nm SHG.

Next, we demonstrate upper-layer $\chi^{(3)}$ tantala operating in concert with lower-layer $\chi^{(2)}$ LN. In Fig. 4c(iv), we present an ultrabroadband, customizable laser-wavelength converter based on OPO in a tantala microresonator followed by SHG in poled LN. Here the pump laser is at 1,076 nm, making primary OPO signal and idler waves at 1,048 nm and 1,107 nm, respectively. The full OPO output is routed from the upper-layer tantala waveguide into the lower-layer LN waveguide, with peak SHG gain, measured at 524 nm, designed to convert the OPO signal. We observe the highest conversion between the 1,048 nm to 524 nm wave, as it is aligned with the QPM peak. We also observe weaker SHG corresponding to conversion of the residual pump laser from 1,076 nm to 538 nm, of the idler from 1,107 nm to 553 nm, and additionally sum-frequency generation of pump-plus-signal and pump-plus-idler OPO waves.

Finally, in Fig. 4c(v), we present tantala–LN devices that enable f–$2f$ self-referencing[40] using cascaded $\chi^{(3)}$ supercontinuum generation[41] in tantala and $\chi^{(2)}$ SHG in LN. The tantala waveguide width, WGW, affords dispersion engineering to optimize supercontinuum generation for operation with custom-wavelength pulsed sources. We show this flexibility by demonstrating two designs, the first with tantala WGW = 650 nm, optimized for operation with a pulsed laser centred at 1,030 nm and the second with WGW = 1,600 nm, optimized for a pulsed laser centred at 1,560 nm (additional experimental details provided in Methods). We calculate the effective nonlinear parameter, $\gamma = 2\pi n_2/\lambda A_{eff}$, where A_{eff} is the effective mode area and n_2 is the nonlinear refractive index of tantala, for these two designs to be 11.0 $W^{-1} m^{-1}$ (1,030 nm pump, WGW = 650 nm) and 3.0 $W^{-1} m^{-1}$ (1,560 nm pump, WGW = 1,600 nm). At the right of Fig. 4c(v), we show a low-pass-filtered (50-MHz corner) radiofrequency spectrum for each device, measured by sending the output light to a photodiode responsive at the second-harmonic waveband. We label the carrier-envelope offset frequency (f_{ceo}) and repetition rate frequency (f_{rep}), which together afford f–$2f$ self-referencing.

Online content

Any methods, additional references, Nature Portfolio reporting summaries, source data, extended data, supplementary information, acknowledgements, peer review information; details of author contributions and competing interests; and statements of data and code availability are available at https://doi.org/10.1038/s41586-026-10379-w.

1. Jung, H. et al. Tantala Kerr nonlinear integrated photonics. *Optica* **8**, 811–817 (2021).
2. Desiatov, B., Shams-Ansari, A., Zhang, M., Wang, C. & Lončar, M. Ultra-low-loss integrated visible photonics using thin-film lithium niobate. *Optica* **6**, 380–384 (2019).
3. Wang, C. et al. Ultrahigh-efficiency wavelength conversion in nanophotonic periodically poled lithium niobate waveguides. *Optica* **5**, 1438–1441 (2018).
4. Spencer, D. T. et al. An optical-frequency synthesizer using integrated photonics. *Nature* **557**, 81–85 (2018).
5. Pfeifle, J. et al. Coherent terabit communications with microresonator Kerr frequency combs. *Nat. Photon.* **8**, 375–380 (2014).
6. Raval, M., Yaacobi, A. & Watts, M. R. Integrated visible light phased array system for autostereoscopic image projection. *Opt. Lett.* **43**, 3678–3681 (2018).
7. Alexander, K. et al. A manufacturable platform for photonic quantum computing. *Nature* **641**, 876–883 (2025).
8. Moss, D. J., Morandotti, R., Gaeta, A. L. & Lipson, M. New CMOS-compatible platforms based on silicon nitride and Hydex for nonlinear optics. *Nat. Photon.* **7**, 597–607 (2013).
9. Pfeiffer, M. H. P. et al. Photonic Damascene process for integrated high-*Q* microresonator based nonlinear photonics. *Optica* **3**, 20–25 (2016).
10. Luke, K., Dutt, A., Poitras, C. B. & Lipson, M. Overcoming Si_3N_4 film stress limitations for high quality factor ring resonators. *Opt. Express* **21**, 22829–22833 (2013).
11. Belt, M., Davenport, M. L., Bowers, J. E. & Blumenthal, D. J. Ultra-low-loss Ta_2O_5-core/SiO_2-clad planar waveguides on Si substrates. *Optica* **4**, 532–536 (2017).
12. Black, J. A. et al. Group-velocity-dispersion engineering of tantala integrated photonics. *Opt. Lett.* **46**, 817 (2021).
13. Jung, H. & Tang, H. X. Aluminum nitride as nonlinear optical material for on-chip frequency comb generation and frequency conversion. *Nanophotonics* **5**, 263–271 (2016).
14. Zhu, D. et al. Integrated photonics on thin-film lithium niobate. *Adv. Opt. Photon.* **13**, 242–352 (2021).
15. Boes, A. et al. Lithium niobate photonics: unlocking the electromagnetic spectrum. *Science* **379**, eabj4396 (2023).
16. Wang, C. et al. Lithium tantalate photonic integrated circuits for volume manufacturing. *Nature* **629**, 784–790 (2024).
17. Karvounis, A., Timpu, F., Vogler-Neuling, V. V., Savo, R. & Grange, R. Barium titanate nanostructures and thin films for photonics. *Adv. Opt. Mater.* **8**, 2001249 (2020).
18. Wang, C. et al. Integrated lithium niobate electro-optic modulators operating at CMOS-compatible voltages. *Nature* **562**, 101–104 (2018).
19. Jankowski, M. et al. Ultrabroadband nonlinear optics in nanophotonic periodically poled lithium niobate waveguides. *Optica* **7**, 40–46 (2020).
20. Younesi, M. et al. Periodic poling with a micrometer-range period in thin-film lithium niobate on insulator. *J. Opt. Soc. Am. B* **38**, 685–691 (2021).
21. Park, T. et al. High-efficiency second harmonic generation of blue light on thin-film lithium niobate. *Opt. Lett.* **47**, 2706–2709 (2022).
22. Komljenovic, T. et al. Photonic integrated circuits using heterogeneous integration on silicon. *Proc. IEEE* **106**, 2246–2257 (2018).
23. Fathpour, S. Heterogeneous nonlinear integrated photonics. *IEEE J. Quantum Electron.* **54**, 1–16 (2018).
24. Nader, N. et al. Heterogeneous tantala photonic integrated circuits for sub-micron wavelength applications. *Optica* **12**, 585–593 (2025).
25. Beeck, C. O. D. et al. III/V-on-lithium niobate amplifiers and lasers. *Optica* **8**, 1288–1289 (2021).
26. Snigirev, V. et al. Ultrafast tunable lasers using lithium niobate integrated photonics. *Nature* **615**, 411–417 (2023).
27. Xiang, C. et al. Laser soliton microcombs heterogeneously integrated on silicon. *Science* **373**, 99–103 (2021).
28. Vanackere, T. et al. Heterogeneous integration of a high-speed lithium niobate modulator on silicon nitride using micro-transfer printing. *APL Photon.* **8**, 086102 (2023).
29. Chang, L. et al. Heterogeneous integration of lithium niobate and silicon nitride waveguides for wafer-scale photonic integrated circuits on silicon. *Opt. Lett.* **42**, 803–806 (2017).
30. Ghosh, S. et al. Wafer-scale heterogeneous integration of thin film lithium niobate on silicon-nitride photonic integrated circuits with low loss bonding interfaces. *Opt. Express* **31**, 12005–12015 (2023).
31. Churaev, M. et al. A heterogeneously integrated lithium niobate-on-silicon nitride photonic platform. *Nat. Commun.* **14**, 3499 (2023).
32. Nagarajan, R. et al. Large-scale photonic integrated circuits. *IEEE J. Sel. Top. Quantum Electron.* **11**, 50–65 (2005).
33. Stojanović, V. et al. Monolithic silicon-photonic platforms in state-of-the-art CMOS SOI processes [Invited]. *Opt. Express* **26**, 13106–13121 (2018).
34. Sacher, W. D., Huang, Y., Lo, G.-Q. & Poon, J. K. S. Multilayer silicon nitride-on-silicon integrated photonic platforms and devices. *J. Lightwave Technol.* **33**, 901–910 (2015).
35. Bose, D. et al. Anneal-free ultra-low loss silicon nitride integrated photonics. *Light Sci. Appl.* **13**, 156 (2024).
36. Carollo, A. R. et al. Amorphous metal oxide mixtures for high-*Q* integrated nonlinear photonics. Preprint at https://arxiv.org/abs/2508.14887 (2025).
37. Lu, X., Rogers, S., Jiang, W. C. & Lin, Q. Selective engineering of cavity resonance for frequency matching in optical parametric processes. *Appl. Phys. Lett.* **105**, 151104 (2014).
38. Yu, S.-P. et al. Spontaneous pulse formation in edgeless photonic crystal resonators. *Nat. Photon.* **15**, 461–467 (2021).

39. Zhang, K. et al. Spectral engineering of optical microresonators in anisotropic lithium niobate crystal. *Adv. Mater.* **36**, 2308840 (2024).
40. Jones, D. J. et al. Carrier-envelope phase control of femtosecond mode-locked lasers and direct optical frequency synthesis. *Science* **288**, 635–639 (2000).
41. Carlson, D. R. et al. Self-referenced frequency combs using high-efficiency silicon-nitride waveguides. *Opt. Lett.* **42**, 2314–2317 (2017).
42. Gayer, O., Sacks, Z., Galun, E. & Arie, A. Temperature and wavelength dependent refractive index equations for MgO-doped congruent and stoichiometric $LiNbO_3$. *Appl. Phys. B* **91**, 343–348 (2008).
43. Tai, C.-Y. et al. Determination of nonlinear refractive index in a Ta_2O_5 rib waveguide using self-phase modulation. *Opt. Express* **12**, 5110–5116 (2004).
44. Ikeda, K., Saperstein, R. E., Alic, N. & Fainman, Y. Thermal and Kerr nonlinear properties of plasma deposited silicon nitride/silicon dioxide waveguides. *Opt. Express* **16**, 12987–12994 (2008).
45. Yi, X., Yang, Q.-F., Yang, K. Y., Suh, M.-G. & Vahala, K. Soliton frequency comb at microwave rates in a high-*Q* silica microresonator. *Optica* **2**, 1078 (2015).
46. Zhou, F. et al. Hybrid-mode-family Kerr optical parametric oscillation for robust coherent light generation on chip. *Laser Photon. Rev.* **16**, 2100582 (2022).
47. Yu, S.-P., Lucas, E., Zang, J. & Papp, S. B. A continuum of bright and dark-pulse states in a photonic crystal resonator. *Nat. Commun.* **13**, 3134 (2022).
48. Rao, A. et al. Actively-monitored periodic-poling in thin-film lithium niobate photonic waveguides with ultrahigh nonlinear conversion efficiency of 4600 $\%W^{-1}cm^{-2}$. *Opt. Express* **27**, 25920–25930 (2019).
49. Chen, P.-K. et al. Adapted poling to break the nonlinear efficiency limit in nanophotonic lithium niobate waveguides. *Nat. Nanotechnol.* **19**, 44–50 (2024).
50. Xin, C. J. et al. Wavelength-accurate and wafer-scale process for nonlinear frequency mixers in thin-film lithium niobate. *Commun. Phys.* **8**, 136 (2025).
51. Black, J. A. et al. Optical-parametric oscillation in photonic-crystal ring resonators. *Optica* **9**, 1183 (2022).
52. Brodnik, G. M., Liu, H., Carlson, D. R., Black, J. A. & Papp, S. B. Nanopatterned parametric oscillators for laser conversion beyond an octave. *Optica* **12**, 337–342 (2025).
53. Zang, J., Liu, H., Briles, T. C. & Papp, S. B. Foundry manufacturing of octave-spanning microcombs. *Opt. Lett.* **49**, 5143–5146 (2024).

Methods

Tantala–LN fabrication

We provide here the details of tantala–LN wafer fabrication (presented in Fig. 2a). Processing begins with commercial, 300-nm-thick magnesium-oxide-doped X-cut LN film on a 3-inch, oxidized silicon wafer. Waveguides in the LN layer are directed along the *y* axis, affording TE polarized operation along the *z* axis. Devices on the LN layer like periodically poled SHG (periodically poled LN) waveguides are processed before tantala deposition. To realize electrodes for periodically poling in LN, we use electron beam lithography to create a pattern in ZEP520A resist, deposit a 100-nm SiO_2 interlayer via atomic layer deposition, then deposit a 100-nm-thick layer of gold–chromium metal. Removing the electron beam lithography resist transfers the pattern to the metal layer via lift-off. Our electrode designs are electrically linked across neighbouring devices to parallelize poling and lend scalability to fabrication. We create poled domains in the LN layer by use of a voltage pulse waveform that exceeds the coercive field strength of LN[20,48], and we monitor the domain inversion using a two-photon microscope. After poling, electrode metals are removed through two selective wet chemical etches at room temperature. First, the gold layer is stripped in Transene TFA and rinsed in deionized water. The chromium layer is then removed in a bath of CR-7 chromium etchant and the wafer is then rinsed again in deionized water. We next lithographically pattern and etch LN waveguides using an argon ion mill to a partial etch depth of approximately 150 nm. To prepare the lower substrate surface for tantala deposition, we proceed by depositing oxide by use of inductively coupled plasma chemical vapour deposition. Because the oxide inherits the topology of the devices and structures present on the lower substrate, we use CMP to planarize the wafer and prepare it for tantala deposition. Following CMP, the substrate resembles a standard, oxide-clad wafer from the perspective of tantala processing, allowing for fabrication to proceed with no modifications from previously developed process flows. We deposit tantala, in this work to a thickness of 570 nm, using room-temperature IBS. We use electron beam lithography to define tantala structures on an 85-nm-thick alumina hardmask layer, followed by etching in a fluorene-based plasma and mask removal. To reduce photorefractive effects in tantala[54], we deposit a 20-nm-thick conformal layer of SiO_2 via atomic layer deposition on the tantala layer and anneal the wafer at 500 °C for 12 h (this anneal step is bypassed for titanium-doped tantala[36]). Finally, tantala–LN wafers are singulated into individual chips using a deep-reactive-ion-etch, which optionally allows for angled facets and other facet geometries.

SHG QPM

We model the QPM curve in the bottom of Fig. 3d by first solving for the wavelength-dependent effective index of the fundamental TE mode across the range of pump and SHG wavelengths using a finite element method mode solver. For material refractive indices, we use Sellmeier data for 5% MgO-doped LN[42] and SiO_2 (ref. 55). The waveguide design comprises a SiO_2 cladding with a 300-nm-thick LN waveguide layer, partially etched to a depth of 150 nm to realize a 2-µm-wide ridge. We use the finite element method wavelength-dependent effective index data to link pump and SHG wavevectors (k_ω and $k_{2\omega}$) with Λ using the QPM relation[56].

$$\Lambda = 2\pi/(2k_\omega - k_{2\omega})$$

SHG insertion loss measurements

Calibrating chip coupling insertion loss is critical for characterizing SHG performance (Fig. 3f). For tantala–LN devices, light is coupled into upper-layer tantala waveguides, routed down into LN for SHG, and routed back into tantala waveguides for output coupling. The tantala waveguides incorporate waveguides with an increasing width to 2.5 µm at the facets to improve mode-matching with optical fibre. Devices pumped at 980-nm and 1,064-nm wavebands used HI1060 lensed fibre with a 2-µm spot size at the input. At the chip output, we edge couple a 50-µm-core-diameter multimode fibre, chosen for broadband compatibility. We independently measure insertion loss for each relevant wavelength (pump and all SHG wavelengths) for fibre-to-chip coupling. To do this, we characterize fibre coupling for symmetric tantala–LN interlayer-routed structures. Using test lasers operating at the experimental pump or SHG wavelength, we first couple light into and out of the chip using matching lensed fibres designed for the test wavelength. We assume symmetric facet loss and record per-facet insertion loss for lensed fibre coupling. We then replace the output fibre with the multimode fibre and measure the additional loss, thereby calibrating the per-wavelength, per-facet loss for either lensed fibre (pump light input) or multimode fibre (SHG light output) coupling configurations for the visible-wavelength SHG measurements. We repeat these same calibrations for the LNOI device. For the 1,550-nm tantala–LN device, we use lensed SMF-28 fibre on both the input and output, and measured SHG light on a visible detector insensitive to the pump (measured rejection >70 dB). The measured insertion losses for the tantala–LN 970 nm to 485 nm SHG device are 5.5 ± 0.3 dB (pump) and 7.5 ± 0.3 dB (signal). The measured insertion losses for the tantala–LN 1,574 nm to 787 nm SHG device are 4.9 ± 0.3 dB (pump) and 5.8 ± 0.3 dB (signal). The measured insertion losses for the LNOI 1,050 nm to 525 nm SHG device are 9.1 ± 0.6 dB (pump) and 11.6 ± 0.6 dB (signal).

SHG power and conversion efficiency

For the visible-wavelength high-power SHG measurements, we filter out the pump light using 2 shortpass optical filters, each cut at a wavelength of 750 nm and specified to have a rejection exceeding 50 dB. We confirm sufficient pump rejection by first measuring the pump laser directly, with and without the filters, observing a rejection exceeding 70 dB and limited by the noise floor of our power meter. We fit the SHG power versus pump data in Fig. 3f to a quadratic curve, assuming no pump depletion, to calculate conversion efficiency in terms of % W^{-1}, then normalize to units of % W^{-1} cm^{-2} using the device lengths reported in text.

Tantala dispersion design

We model GVD in Fig. 4a by first solving for the effective index as a function of wavelength of the TE0 mode using a finite element method mode solver. For the material refractive index of tantala, we use a Sellmeier fit from published ellipsometry data measured on the tantala photonics platform[12]. We use the calculated effective index data to solve for discrete resonator mode frequencies, ω, with corresponding integer mode numbers, m, for a given microresonator ring radius. For a selected pump mode, m_0, we then calculate integrated dispersion[57] using

$$\begin{aligned}\omega(\mu) &= \omega_0 + D_1\mu + D_2\mu^2/2 + D_3\mu^3/6 + \ldots \\ &= \omega_0 + D_1\mu + D_{\text{int}}\end{aligned}$$

where μ is the mode number with respect to the pump ($\mu = m - m_0$). In this description, $D_1/2\pi$ is the free spectral range. D_{int} thereby describes the departure of mode frequencies from a linear, free-spectral-range-spaced grid. $D_2/2\pi$ is the GVD parameter plotted in Fig. 4a.

Tantala nonlinear testing conditions

We provide here experimental conditions that accompany the data presented in Fig. 4c. Figure 4c(i) shows a microresonator OPO for a device with a measured loaded Q of 0.43 M. The device was pumped at 968 nm with an on-chip pump power of 44 mW. Figure 4c(ii) presents dark-pulse spectra of two normal dispersion PhCR devices. The 980-nm device (left) was measured to have loaded Q of 2.0 M and was operated with an on-chip pump power of 89 mW. The 1,550-nm device (right) was measured to have loaded Q of 2.65 M and was operated with on-chip pump power of 100 mW. Figure 4c(iv) presents a microresonator OPO cascaded to LN for SHG. The microresonator was measured to have loaded *Q* of 0.62 M and was operated with on-chip pump power of approximately 50 mW. Figure 4c(v) presents supercontinuum generation in tantala waveguides cascaded to LN SHG. For the 1,030-nm device (blue), the chip insertion loss was measured to be 6 dB per facet and the pump was a pulsed laser with pulse width 150 fs, average power 150 mW and repetition rate of 100 MHz. For the 1,560-nm data (orange), the insertion loss was measured to be 5 dB per facet and the pump laser had pulse width 150 fs, average power 58 mW and repetition rate of 75 MHz.

Data availability

The data necessary to evaluate the conclusions of this work are provided in the paper. Requests can be accommodated by contacting the corresponding author.

54. Fazio, M. A. et al. Structure and morphology of low mechanical loss TiO_2-doped Ta_2O_5. *Opt. Mater. Express* **10**, 1687–1703 (2020).
55. Malitson, I. H. Interspecimen comparison of the refractive index of fused silica. *J. Opt. Soc. Am.* **55**, 1205–1209 (1965).
56. Boyd, R. W. *Nonlinear Optics* 4th edn (Academic Press, 2020).
57. Fujii, S. & Tanabe, T. Dispersion engineering and measurement of whispering gallery mode microresonator for Kerr frequency comb generation. *Nanophotonics* **9**, 1087–1104 (2020).

Acknowledgements We thank S. Yeola and N. Chauhan for internal review of the paper. This research has been funded by the DARPA LUMOS programme HR0011-20-2-0046, AFOSR FA955020-1-0004 Project Number 19RT1019, NSF Quantum Leap Challenge Institute Award OMA - 2016244, and NIST. This work is a contribution of the US Government and is not subject to US copyright. Mention of specific companies or trade names is for scientific communication only and does not constitute an endorsement by NIST.

Author contributions G.M.B., G.S., L.M.W., J.Z., A.R.C. and D.R.C. conducted the experiments. G.M.B., G.S., L.M.W., J.Z., D.R.C. and J.A.B. designed and simulated devices and analysed experimental data. D.R.C., G.S., A.D. and J.Z. fabricated the devices. G.M.B., L.M.W. and S.B.P. prepared the paper. All authors reviewed the paper. S.B.P. supervised the project and acquired funding.

Competing interests The authors declare no competing interests.

Additional information
Supplementary information The online version contains supplementary material available at https://doi.org/10.1038/s41586-026-10379-w.

Correspondence and requests for materials should be addressed to Grant M. Brodnik.

Peer review information *Nature* thanks Daniele Melati and the other, anonymous, reviewer(s) for their contribution to the peer review of this work. Peer reviewer reports are available.